Model for the Formation of Longshore Sand Ridges on the Continental Shelf: The Interaction of Internal Waves and the Bottom Topography

Juan Mario Restrepo

Mathematics and Computer Science Division

Argonne National Laboratory, Argonne IL U.S.A. 60439

Jerry L. Bona

Mathematics Department

The Pennsylvania State University, University Park PA U.S.A. 16802

January 5, 1994

Abstract

Longshore sand ridges are frequently observed to occur on the continental shelf where the overlying ocean is stratified. This study formulates a model for the formation and evolution of three-dimensional longshore sand ridges on the continental shelf. The model is based on the interaction of interfacial, weakly nonlinear waves in a stratified ocean with the sedimentary bottom topography.

1 Introduction

Sand ridges are underwater barlike features composed of loose granular sediment. Sand ridges hundreds of meters long and up to a few meters high are usually found in groups, arranged in more or less parallel rows separated from each other by hundreds of meters oriented normal to the direction in which the overlying water waves propagate.

Shallow-water, weakly nonlinear interfacial waves appear as highly coherent groups having well-defined wavelength and are observed propagating shoreward on a density stratification, such as the picnocline. Their crests are generally oriented along isobaths [Apel1979,Baines1981]. Their wavelengths range from 200 to 1600 meters, depending on the depth, which can be considerably larger than the local water column depth. An estimate of the energy contained in the larger ones is in the order of 0.1 MJ/m^2. They have been seen to appear twice a day in some areas, coinciding with the tidal cycle, and originate mostly in places where there are sharp changes in the bottom topography, such as on the edge of the continental shelf. Since the contribution of coriolis forces in this problem is negligible (i.e., the wave periods for the waves under consideration range between fractions of a minute and an hour), the sole forcing agent is gravitational. As the density stratification collapses in the shallower reaches of the shelf, the water column is no longer able to support an internal wave. Hence, in our formulation of the model for the internal wave case, we assume that the wave field is strictly unidirectional.

Referring to Figure 1, we envision infragravity waves coming into the purview of the model at the line $x = 0$, where the long waves begin "feeling" the bottom

topography. The shoreward direction, x, increases as the wave travels shoreward. The spanwise direction, given by y, is approximately parallel to the line of constant phase of the incoming waves. The waves propagate shoreward, possibly at an angle with respect to the prevailing direction of maximum gradient of the bottom topography. The extent of the model is limited in the longshore direction by the disintegration of the interface supporting the internal waves, by the approach to the breaking zone, by any singularity in the depth, or by significant energy transfer from low to high frequencies, reflecting a severe imbalance between nonlinear and dispersive effects in the wave train. The spanwise direction is limited by the same sort of issues. The absence of a reflected component originating, perhaps, in the

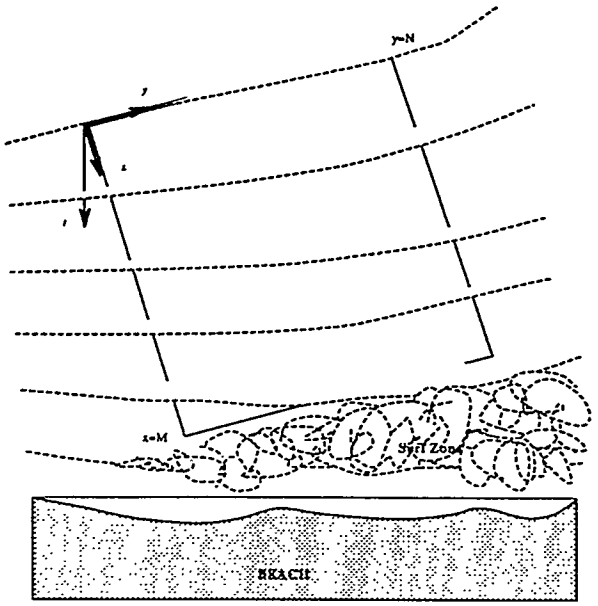

Figure 1: Aerial view of the problem

shoaling region may be justified by the collapse of the density stratification in the shallower reaches of the shelf, the water column no longer being able to support an internal wave.

Field data from the continental shelf suggests that there are two time scales: a fast time scale t, which measures the evolution of the fluid quantities, and a long time scale T which measures the evolution of the bottom topography. In addition, the data suggests that the typical height and slope of the longshore sand ridges, represented in this study by the function h, is such that $\varepsilon = O(\nabla^n h) = O(\alpha)$, where α is a small-valued parameter typical of the ratio of the amplitude of the water waves to the depth of the water column below the fluid interface in an assumed two-density fluid. Furthermore, the type of longshore sand ridge under consideration is such that longshore spatial variation is larger than the spatial variations of the fluid quantities. It is proposed that the sand ridge shoreward variation be $X = \alpha x$. Hence, two scales of shoreward variation exist, so that

$$\partial_x \to \partial_x + \alpha \partial_X. \tag{1}$$

The bottom in scaled variables may be represented by

$$h(X, y, T) = 1 + \varepsilon f(X, y, T), \tag{2}$$

where the function $f = O(1)$.

The plan of this paper is as follows. In Section 2, the main hydrodynamical issues for the internal waves are considered, as well as the mass transport problem. In order to illustrate the main features of the model, section 3 presents a few computed examples, followed in Section 4 by some closing remarks and suggestions for future work.

2 The Model

In this section we discuss both the hydrodynamics of the model and the mass transport problem.

2.1 The Hydrodynamics

We begin by developing the Hamiltonian formulation to the two-fluid internal wave problem, relying on Bowman's work [Bowman1986]. As illustrated in Figure 2, the domain is described by $\Omega_1 \approx \mathbf{R}^2 \times [-H, \eta]$, and $\Omega_2 = \mathbf{R}^2 \times [\eta, D]$. The lower layer (1) has a uniform density ρ_1, and the upper layer (2) a density $\rho_2 < \rho_1$. The fluid is subjected solely to gravitational forcing. The velocity field is now given in each layer by $(\mathbf{u}, w)_i$, where the subscript refers to layer 1 or 2. The interface between the two fluids is given by $z = \eta(\mathbf{r}, t)$ and the bottom by $z = -H(\mathbf{r}, T)$. The transverse variable $\mathbf{r} = (x, y)$, where x increases shoreward and y is the spanwise coordinate.

The fluid is assumed incompressible and irrotational in each layer. In terms of a scalar potential, the velocity is given by

$$(\mathbf{u}, w)_i = \nabla_3 \phi_i. \tag{3}$$

From conservation of mass, the equations of motion within the fluid are

$$\Delta_3 \phi_i = 0, \text{ in } \Omega_i. \tag{4}$$

At the interface, the pressure is continuous; hence the dynamical boundary

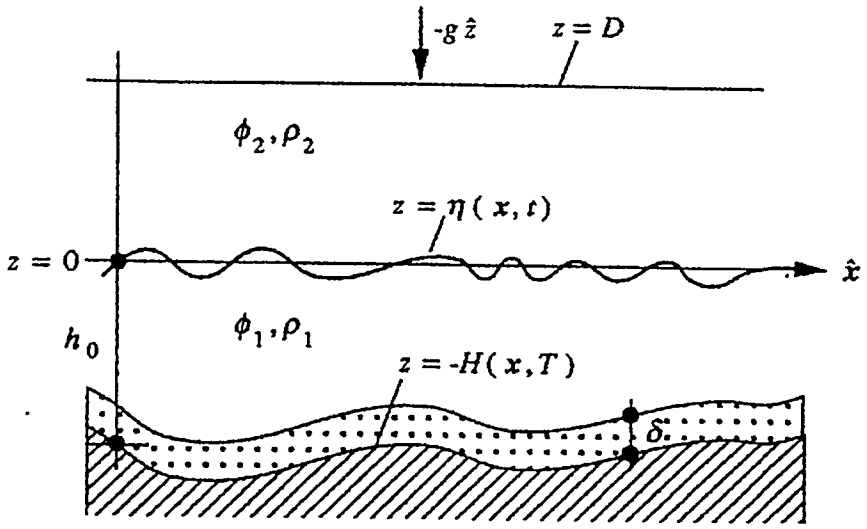

Figure 2: Side view, internal wave problem

condition is

$$\phi_{i,t} = -\frac{1}{2}|\nabla_3 \phi_i|^2 - g\rho_i \eta, \text{ at } z = \eta. \tag{5}$$

The bottom, which is assumed impermeable, has a normal velocity that agrees with that of the fluid. Thus

$$\phi_{1,z} = -\nabla H \cdot \nabla \phi_1 \text{ at } z = -H. \tag{6}$$

The kinematic condition on the interface is $\frac{D(z-\eta)}{Dt} = 0$. or

$$\phi_{i,z} = \eta_t + \nabla \phi_i \cdot \nabla \eta \text{ at } z = \eta. \tag{7}$$

Finally, we make the simplifying "rigid-lid" assumption

$$\phi_{2,z} = 0, \text{ at } z = D \tag{8}$$

at the constant air-water interface.

With conjugate variables η and $\mathbf{U} \equiv \rho_2 \nabla\phi_2 - \rho_1 \nabla\phi_1$ the Hamiltonian system that yields the description of the dynamics of the internal waves takes the form

$$\begin{aligned} \eta_t &= -\nabla\cdot(\frac{\delta E}{\delta \mathbf{U}}) \\ \mathbf{U}_t &= -\nabla(\frac{\delta E}{\delta \eta}), \end{aligned} \tag{9}$$

where the Hamiltonian E is numerically equal to the sum of the potential and the kinetic energy for this problem.

The potential energy is simply

$$V = \int\limits_{\mathbf{R}^2} d^2r \frac{1}{2} g(\rho_1 - \rho_2)\eta^2. \tag{10}$$

The total kinetic energy is the sum of contributions from both layers; thus

$$K = \rho_1 \int\limits_{\mathbf{R}^2} d^2r \int\limits_{-H}^{\eta} \frac{1}{2} |\nabla_3 \phi_1|^2 dz + \rho_2 \int\limits_{\mathbf{R}^2} d^2r \int\limits_{-\eta}^{D} \frac{1}{2} |\nabla_3 \phi_2|^2 dz = K_1 + K_2. \tag{11}$$

Define the parameters $\alpha \ll 1$, and $\beta \ll 1$. Assume that $O(\alpha) \sim O(\beta^2)$, and take $H = O(1)$, $\nabla H = O(\alpha)$, $\eta = O(\alpha)$, $\Phi = O(\alpha)$. Further, consider the differentiations $\partial_z, \partial_t, \nabla = O(\beta)$.

Referring to the results from [Restrepo & Bona1993b], we calculate the kinetic

energy in the lower layer using an approximation for the velocity potential,

$$\begin{aligned} \phi_1(\mathbf{r},z,t) = \quad & \Phi_1(\mathbf{r},t) \quad - \quad \tfrac{1}{2}z^2\nabla^2\Phi_1(\mathbf{r},t) \quad - \quad z\nabla\cdot(H\nabla\Phi_1(\mathbf{r},t)), \\ & O(\alpha) \qquad\qquad O(\alpha\beta^2) \qquad\qquad O(\alpha\beta^2) \end{aligned}$$

so that

$$K_1 = \rho_1 \int_{\mathbf{R}^2} d^2r\{\frac{1}{2}(H+\eta)(\nabla\Phi_1)^2 + \frac{H}{2}(\nabla H\cdot\nabla\Phi_1)^2 - \frac{H^3}{6}(\nabla^2\Phi_1)^2\}, \tag{12}$$

which is an expression of $O(\alpha^3\beta^2)$ and $O(\alpha^2\beta^4)$.

The boundary condition given by Equation (8) can be exploited to find K_2 as a surface integral. Using Green's theorem and assuming that the gradients of the potential tend to zero as $|\mathbf{r}| \to \infty$, we have

$$K_2 = -\rho_2 \int_{\mathbf{R}^2} d^2r\nabla\Phi_1\nabla\Phi_2. \tag{13}$$

Define the pseudo-differential operator $G \equiv -k\coth(HkD)$. Its precise structure is a result of satisfying the boundary conditions on the interface and on the ocean surface. Adding the expressions for K_1 and K_2, using the definition of $\mathbf{U}$, and the operator G, we obtain as the total kinetic energy

$$K = \frac{1}{2}\int_{\mathbf{R}^2} d^2r\{\frac{1}{\rho_1}(H+\eta)\mathbf{U}^2 + \frac{H^2\rho_2}{\rho_1^2}\mathbf{U}\cdot G\mathbf{U} + \frac{\rho_2 H}{\rho_1^2}(\nabla H\cdot\mathbf{U})^2\} + O(\alpha^3\beta^2), \tag{14}$$

or rearranging,

$$K = \frac{1}{2}\int\limits_{\mathbf{R}^2} d^2r\{\frac{1}{\rho_1}[(H+\eta) - \frac{H^2\rho_2}{\rho_1^2 D}]\mathbf{U}^2 + \frac{H^2\rho_2}{\rho_1^2}\mathbf{U}\cdot M\mathbf{U} + \frac{\rho_2 H}{\rho_1^2}(\nabla H\cdot\mathbf{U})^2\} + O(\alpha^3\beta^2), \tag{15}$$

where $M = \frac{I}{D} + G = \frac{1}{D} - k\coth(HkD)$.

Depending on the size of D/λ, there are three physically distinct possibilities:

- If $D/\lambda \ll 1$, then $\mathbf{U}\cdot M\mathbf{U} = O(\alpha^2 D/\lambda^2)$, and $M \approx 1/D - \frac{D\nabla^2}{3}$. For this case, the terms $\eta\mathbf{U}\cdot\mathbf{U}$ and $\mathbf{U}\cdot M\mathbf{U}$ balance if $\alpha^2 D/\lambda^2 \sim 1$. A Boussinesq system is obtained.

- If $D/\lambda \sim 1$, then $\mathbf{U}\cdot M\mathbf{U} = O(\alpha^2/\lambda)$. For this case, if $\alpha\lambda^2/D \sim 1$, the result is the intermediate long-wave equation.

- If $D/\lambda \gg 1$, then $\mathbf{U}\cdot M\mathbf{U} = O(\alpha^2/\lambda)$, and $M \approx |k|$. If $\alpha\lambda \sim 1$, the outcome is the Benjamin-Ono equation.

Note that this last case corresponds to a very deep upper layer, lying over a thinner lower layer, and hence is not considered relevant in this study.

By substituting the expressions for the potential and kinetic energy, Equations (10) and (15), into Equation (9), the general equation for the dynamics of the internal wave field is obtained:

$$\begin{aligned} \eta_t &= -\nabla\cdot\{[\tfrac{1}{\rho_1}(H+\eta) - \tfrac{H^2\rho_2}{\rho_1^2 D}]\mathbf{U}\} - \tfrac{\rho_2}{\rho_1^2}\nabla\cdot\{H(\nabla H)^2\mathbf{U} + H^2 M\mathbf{U}\} \\ \mathbf{U}_t &= -\nabla\cdot\{\tfrac{1}{2\rho_1^2}\mathbf{U}\cdot\mathbf{U} + (\rho_1 - \rho_2)g\eta\}. \end{aligned} \tag{16}$$

The result from linear theory may be recovered by neglecting second- and higher-

order terms in Equation (16). The solutions proportional to $\exp\{i(kx-\omega t)\}$ satisfy

$$\begin{aligned} \omega\eta &= (\tfrac{1}{\rho_1} - \tfrac{\rho_2 H}{\rho_1^2 D} + \tfrac{\rho_2 HM}{\rho_1^2})kHU \\ \omega U &= k(\rho_1 - \rho_2)g\eta. \end{aligned} \tag{17}$$

Thus,

$$c^2 \equiv \frac{\omega^2}{k^2} = \frac{g(\rho_1 - \rho_2)}{\rho_1}[1 - \frac{\rho_2}{\rho_1} Hk \coth(kD)]. \tag{18}$$

The relevant case in this study is the first one. The Boussinesq system is then

$$\begin{aligned} \eta_t &= -\nabla\cdot\{\tfrac{1}{\rho_1}(H+\eta)\mathbf{U}\} - \tfrac{\rho_2}{\rho_1^2}\nabla\cdot\{H(\nabla H)^2\mathbf{U} + \tfrac{1}{3}H^2 D\nabla\nabla\cdot\mathbf{U}\} \\ \mathbf{U}_t &= -\nabla\cdot\{\tfrac{1}{2\rho_1^2}\mathbf{U}\cdot\mathbf{U} + (\rho_1 - \rho_2)g\eta\}. \end{aligned} \tag{19}$$

Equation (16) may be shown to be linearly unstable [Bona1975]. To circumvent this problem, we carry out an ad-hoc procedure that "regularizes" the equation. The lowest-order relations

$$\begin{aligned} \eta_t &= -\nabla\cdot\{\tfrac{1}{\rho_1}H\mathbf{U}\} \\ \mathbf{U}_t &= -\nabla\{(\rho_1 - \rho_2)g\eta\} \end{aligned} \tag{20}$$

are used to modify the troublesome parts of the dispersive terms to get the regularized model for the hydrodynamics relevant in this study. namely,

$$\begin{aligned} \eta_t &= -\nabla\cdot\{\tfrac{1}{\rho_1}(H+\eta)\mathbf{U}\} + \tfrac{D\rho_2}{3\rho_1^2}\nabla\cdot[\nabla(H\eta_t)] \\ \mathbf{U}_t &= -\nabla\{\tfrac{1}{2\rho_1^2}\mathbf{U}\cdot\mathbf{U} + (\rho_1 - \rho_2)g\eta\}. \end{aligned} \tag{21}$$

Let $\gamma \equiv \frac{(\rho_1-\rho_2)}{\rho_1}$ be the Boussinesq parameter, and let the typical thickness of

the lower layer be h_0. The scaling adopted here is

$$t \leftarrow \frac{\sqrt{gh_0}t}{\lambda} \quad \mathbf{U} \leftarrow \frac{\sqrt{h_0}\mathbf{U}}{\rho_1\sqrt{g}a} \quad \eta \leftarrow \eta/a \quad h \leftarrow \frac{H}{h_0} \quad d \leftarrow \frac{D}{h_0} \quad \mathbf{r} \leftarrow \frac{\mathbf{r}}{\lambda}, \tag{22}$$

where the convention *new* $\leftarrow$ *scale* $\times$ *old* is being used. Equation (21) is, in scaled variables,

$$\begin{aligned} \eta_t + \nabla\cdot\{\tfrac{1}{\rho_1}(h+\alpha\eta)\mathbf{U}\} - d\beta^2\tfrac{\rho_2}{3\rho_1}\nabla\cdot[\nabla(h\eta_t)] &= 0 \\ \mathbf{U}_t + \nabla\{\tfrac{1}{2}\mathbf{U}\cdot\mathbf{U} + \gamma\eta\} &= 0. \end{aligned} \tag{23}$$

Additionally, the spanwise variables are scaled to reflect the weak spanwise dependence of the waves:

$$y \leftarrow \alpha^{1/2}y \qquad \hat{y}\cdot\mathbf{u} \leftarrow \alpha^{-1/2}\hat{y}\cdot\mathbf{u}. \tag{24}$$

The substitution of a uniform expansion of the form

$$\begin{aligned} \eta &= f_0 + \alpha^1 f_1 + \alpha^2 f_2 + \cdots \\ \mathbf{U} &= \mathbf{g}_0 + \alpha^1\mathbf{g}_1 + \alpha^2\mathbf{g}_2 + \cdots \end{aligned} \tag{25}$$

into Equation (23), followed by matching order by order yields the internal wave equation to lowest orders in α.

Explicitly, after crossdifferentiating Equation (23),

$$\begin{aligned} \alpha^0: &\quad \mathcal{L}\eta_0 = 0 \\ \alpha^1: &\quad \mathcal{L}\eta_1 = \mathcal{G}_1(\eta_0, u_0, v_0, G; x, X, y, t) \\ \alpha^2: &\quad \mathcal{L}\eta_2 = \mathcal{G}_2(\eta_0, u_0, v_0, \eta_1, u_1, v_1, G; x, X, y, t) \end{aligned} \tag{26}$$

where

$$\begin{aligned} \mathcal{L} &= \partial_{tt} - \gamma\partial_{xx} - d\frac{\beta^2\rho_2\partial_{xxtt}}{3\rho_1}, \\ G &= \frac{\varepsilon}{\alpha}f(X,y,T). \end{aligned} \tag{27}$$

The inhomogeneous term in the first-order equation is given by

$$\begin{aligned} \mathcal{G}_1 &= (\gamma + d\frac{\beta^2\rho_2\partial_{tt}}{3\rho_1})\eta_{0yy} + G(\gamma + d\frac{2\beta^2\rho_2\partial_{tt}}{3\rho_1})\eta_{0xx} + 2(\gamma + d\frac{\beta^2\rho_2\partial_{tt}}{3\rho_1})\eta_{0xX} \\ &\quad +(u_0^2/2)_x - (u_0\eta_0)_{xt}. \end{aligned} \tag{28}$$

Assuming that lowest-order modal expansion for the surface velocity is of the form

$$u_0(x,X,y,t) = \sum_{j=1}^{2} a_j(X,y)e^{i(k_jx-\omega_jt)} + c.c.., \tag{29}$$

and making use of the lowest-order relation $u_{0t} + \gamma\nabla\eta_0 = 0$ to obtain the surface amplitude

$$\eta_0(x,X,y,t) = \sum_{j=1}^{2} \frac{\omega_j}{\gamma k_j} a_j(X,y)e^{i(k_jx-\omega_jt)} + c.c. \tag{30}$$

we are able to obtain a lowest order description of the internal waves. A solution of the above-mentioned form is possible if the relation between the frequency and wavenumber of the modes satisfies the dispersion relation

$$\omega_j^2 - \frac{k_j^2}{\gamma + d\beta^2\frac{\rho_2 k_j^2}{3\rho_1}} = 0. \tag{31}$$

The solution must also satisfy a compatibility condition. Since the linear operator $\mathcal{L}$ in Equation (26) appears in every order, and terms of lower order appear in the inhomogeneous part, secular terms arise. It is an artifice of having truncated the expansion and is typified by the possibility of blowup due to resonance. This

resonance condition for j^{th} interacting waves is

$$\begin{aligned} k_j \pm \cdots \pm k_2 \pm k_1 &= 0 \\ \omega_j + \cdots + \omega_2 + \omega_1 &= 0, \end{aligned} \tag{32}$$

where the wavenumbers and corresponding frequencies obey the dispersion relation given by Equation (31). In the scaling adopted in this study the $O(k_j) = O(\omega_j)$.

As discussed in [Restrepo & Bona1993b], only weak resonance is to be expected. Particular attention is given in this study to the weakly resonant triad case in which $k_2 = 2k_1 - \delta$, $\omega_2 = 2\omega_1$, where the detuning parameter $\delta \leq 0$. The compatibility condition is

$$\frac{jk_1}{2\pi} \int_{X_0}^{X_0+2\pi/jk_1} e^{\pm ijk_1 x}(\mathcal{G}_j + \mathcal{G}_j^*)dx = 0, \text{where } j = 1, 2, 3..., \tag{33}$$

starred quantities conjugated. Substituting Equations (29) and (30) into Equation (26) and applying the compatibility condition, we obtain the equations for spatial variation of the first two modal amplitudes

$$\begin{aligned} a_{1x} + i\varepsilon f D_1 E_1 a_1 - i\alpha F_1 a_{1yy} + i\alpha D_1 S_1 e^{-i\delta x} a_1^* a_2 &= 0 \\ a_{2x} + i\varepsilon f D_2 E_2 a_2 - i\alpha F_2 a_{2yy} + i\alpha D_2 S_2 e^{+i\delta x} a_1^2 &= 0, \end{aligned} \tag{34}$$

to $O(\delta/X)$. The constants are

$$\begin{aligned} D_j &= 1/2(1 - d\frac{\rho_2\beta^2\omega_j^2}{3\rho_1}) \\ E_j &= k_j(\gamma - d\frac{2\rho_2\beta^2\omega_j^2}{3\rho_1} \\ F_j &= 1/2k_j \\ S_1 &= \frac{k_2-k_1}{\omega_1}\{k_2 - k_1 + \frac{\omega_1}{\gamma}(\frac{\omega_1}{k_1} + \frac{\omega_2}{k_2})\} \\ S_2 &= \frac{2}{\omega_2}k_1^2 + 2\omega_1^2. \end{aligned} \tag{35}$$

For resonant quartets the relation among the frequency and wavenumbers $\omega_j = j\omega_1$, $k_2 = 2k_1 - \delta$, and $k_3 = 3k_1 - \Delta$ is given by the dispersion relation. The procedure is the same as the two-mode case and yields

$$\begin{aligned} a_{1x} + i\varepsilon f D_1 E_1 a_1 - i\alpha F_1 a_{1yy} + i\alpha D_1 S_{211} e^{-i\delta x} a_1^* a_2 + i\alpha D_1 S_{321} e^{i\Delta x} a_2^* a_3 &= 0 \\ a_{2x} + i\varepsilon f D_2 E_2 a_2 - i\alpha F_2 a_{2yy} + i\alpha D_2 S_2 e^{+i\delta x} a_1^2 + i\alpha D_2 S_{312} e^{i\Delta x} a_1^* a_3 &= 0 \\ a_{3x} + i\varepsilon f D_3 E_3 a_3 - i\alpha F_3 a_{3yy} + i\alpha D_3 S_3 e^{-i\Delta x} a_1 a_2 &= 0, \end{aligned} \tag{36}$$

to $O(\delta/X)$. The constants are, with subscripts $1, 2$, or 3,

$$\begin{aligned} D_j &= 1/2(1 - \frac{d\rho_2\beta^2\omega_j^2}{3\rho_1}) \\ E_j &= k_j(\gamma - \frac{2d\rho_2\beta^2\omega_j^2}{3\rho_1}) \\ F_j &= 1/2k_j \\ S_3 &= \frac{k_2+k_1}{\omega_3}\{k_2 + k_1 + \frac{3\omega_1}{\gamma}(\frac{\omega_1}{k_1} + \frac{\omega_2}{k_2})\} \\ S_2 &= \frac{2}{\omega_2}k_1^2 + 2\omega_1^2 \\ S_{ijl} &= \frac{k_i-k_l}{l\omega_1}\{k_i - k_j + \frac{l\omega_1}{\gamma}(\frac{\omega_i}{k_i} + \frac{\omega_j}{k_j})\}. \end{aligned} \tag{37}$$

In this study we restrict our attention to the triad case.

2.2 The Mass Transport Problem

The drift velocity is the second-order steady state flow in the sediment-laden boundary layer that hugs the bottom topography generated by the passage of the overlying water waves. The boundary layer is assumed to have a characteristic thickness $\delta_{bl} \ll h_0$. The sediment in the boundary layer is assumed to move from place to place at a rate equal to the drift velocity.

In order to compute the drift velocity, an explicit expression for the fluid velocity immediately outside of the sediment-laden boundary layer is required. From inviscid theory, in scaled variables, the shoreward velocity is explicitly

$$\begin{aligned} U_b &\equiv \gamma \hat{x}\cdot\mathbf{U}(\mathbf{r},-h,t) \\ &= \gamma u(\mathbf{r},t) - \gamma\beta^2\{-h[(hu_{xx}(\mathbf{r},t)) + \alpha(hv_{xy}(\mathbf{r},t))] + \tfrac{1}{2}h^2(u_{xx}(\mathbf{r},t) + \alpha v_{xy}(\mathbf{r},t))\}, \end{aligned} \tag{38}$$

and the span-wise velocity

$$\begin{aligned} V_b &\equiv \gamma \hat{y}\cdot\mathbf{U}(\mathbf{r},-h,t) \\ &= \gamma v(\mathbf{r},t) - \gamma\beta^2\{-h[(hu_{xy}(\mathbf{r},t)) + \alpha(hv_{yy}(\mathbf{r},t))] + \tfrac{1}{2}h^2(u_{xy}(\mathbf{r},t) + \alpha v_{yy}(\mathbf{r},t))\} \end{aligned} \tag{39}$$

in the neighborhood of the boundary layer. The bottom velocities to lowest order are

$$\begin{aligned} U_{0b} &= \gamma(u_0 + \beta^2\tfrac{h^2}{2}u_{0xx}) \\ &= \textstyle\sum_{j=1}^{2} C_j a_j(X,y)e^{i(k_j x-\omega_j t)} + c.c. \\ V_{0b} &= \gamma v_0 + \gamma\beta^2\tfrac{(h^2)_y}{2}u_{0x} + \gamma\beta^2\tfrac{h^2}{2}u_{0xy} \\ &= -i\textstyle\sum_{j=1}^{2}\tfrac{1}{k_j}[C_j a_{jy}(X,y) + i\gamma\beta^2\tfrac{k_j}{2}(h^2)_y]e^{i(k_j x-\omega_j t)} + c.c., \end{aligned} \tag{40}$$

where $C_j = \gamma(1-\beta^2 k_j^2\tfrac{h^2}{2})$.

As shown in [Restrepo & Bona1993b], for high Reynolds flows, the equations of motion in the boundary layer are given by

$$\begin{aligned}
\beta u_t + \alpha\beta[uu_x + \alpha v u_y] + \alpha w u_n &= -\frac{\beta}{\alpha} p_x + u_{nn} \\
\beta v_t + \alpha\beta[uv_x + \alpha v v_y] + \alpha w v_n &= -\frac{\beta}{\alpha} p_y + v_{nn} \\
p_n &= O(\delta_{bl}) \\
\beta(u_x + \alpha v_y) + w_n &= 0,
\end{aligned} \tag{41}$$

where the vertical coordinate $\delta_{bl} n = z + h$. A locally flat bed has been assumed. The following boundary data used to solve Equation (41) is

$$u = v = w = 0 \qquad \text{at } n = 0 \tag{42}$$

and

$$\begin{aligned}
u &\to U_b \\
v &\to V_b, \qquad n \to \infty.
\end{aligned} \tag{43}$$

The velocity (U_b, V_b) immediately outside of the layer gives rise to the following pressure gradients:

$$\begin{aligned}
-\frac{\beta}{\alpha} p_x &= \beta U_{bt} + \alpha\beta(U_b U_{bx} + \alpha V_b U_{by}) \\
-\frac{\beta}{\alpha} p_y &= \beta V_{bt} + \alpha\beta(U_b V_{bx} + \alpha V_b V_{by}).
\end{aligned} \tag{44}$$

All the required information to solve for the velocities in the boundary layer is thus

at hand. Performing the expansion

$$\begin{aligned} u &= \tilde{u}_0 + \alpha\tilde{u}_1 \cdots \\ v &= \tilde{v}_0 + \alpha\tilde{v}_1 \cdots, \end{aligned} \tag{45}$$

we obtain the lowest-order boundary layer equations

$$\begin{aligned} \beta\tilde{u}_{0t} - \tilde{u}_{0nn} &= \beta U_{0bt} \\ \beta\tilde{v}_{0t} - \tilde{v}_{0nn} &= \beta V_{0bt} \\ p_{0n} &= 0 \\ \beta\tilde{u}_{0x} + \tilde{w}_{0n} &= 0. \end{aligned} \tag{46}$$

A solution of Equation (46) of the form

$$\tilde{u}_l = \sum_{j=1}^{2} \alpha^l P_l(x, y, n) e^{i(k_j x - \omega_j t)} + c.c., \tag{47}$$

with a similar representation for $\tilde{v}_l$, subject to the boundary conditions given by Equations (42) and (43), is found by integrating Equation (46). The result is

$$\begin{aligned} \tilde{u}_0 &= \textstyle\sum_{j=1}^{2} C_j a_j (1 - e^{-n\Lambda_j}) e^{i(k_j x - \omega_j t)} + c.c. \\ \tilde{v}_0 &= i \textstyle\sum_{j=1}^{2} k_j (\beta^2 (h^2)_y a_j / 2 - C_j a_{jy} / k_j^2)(1 - e^{-n\Lambda_j}) e^{i(k_j x - \omega_j t)} + c.c. \\ \tilde{w}_0 &= i\beta \textstyle\sum_{j=1}^{2} k_j C_j a_j (1 - n\Lambda_j - e^{-n\Lambda_j})/\Lambda_j e^{i(k_j x - \omega_j t)} + c.c., \end{aligned} \tag{48}$$

where $\Lambda_j = (1 - i)\sqrt{\beta\omega_j/2}$. The vertical velocity $\tilde{w}$ is found by integrating the continuity equation.

The drift velocity [Longuett-Higgins1953,Restrepo1992] is given by

$$\begin{aligned} \mathcal{U} &= \langle u_1 \rangle + \langle \int^t \tilde{u}_0 d\tilde{t} \tilde{u}_{0x} \rangle + \langle \int^t \tilde{w}_0 d\tilde{t} \tilde{u}_{0n} \rangle \\ \mathcal{V} &= \langle v_1 \rangle + \langle \int^t \tilde{u}_0 d\tilde{t} \tilde{v}_{0x} \rangle + \langle \int^t \tilde{w}_0 d\tilde{t} \tilde{v}_{0n} \rangle. \end{aligned} \tag{49}$$

It is assumed that the viscous boundary layer is sediment-laden; composed of cohesionless, rarely interacting sand particles.

The mass transport equation [Restrepo & Bona1993b] is

$$\frac{\partial h(x,y,T)}{\partial T} = \frac{K}{\rho_0}(\mu_x + \nu_y), \tag{50}$$

where ρ_0 is the mean sediment concentration and μ and ν are the shoreward mass flux and the longshore mass flux, respectively:

$$\begin{aligned} \mu &\equiv \int_0^{\delta_{bl}} \rho(x,z') \mathcal{U}(x,z')) dz' \\ \nu &\equiv \int_0^{\delta_{bl}} \rho(x,z') \mathcal{V}(x,z')) dz'. \end{aligned} \tag{51}$$

Note that when weak y dependence scaling is adopted in Equation (50) the longshore mass flux is $O(\alpha)$ smaller than the shoreward flux.

In the remainder of this study, we assume, for simplicity, that the sediment concentration is constant and equal to ρ_0 in the boundary layer. In terms of Equation (49), and upon use of Equation (51), the mass flux components, to lowest order, are

$$\mu = \sum_{j=1}^{2} \frac{2k_j C_j^2 |a_j|^2}{\omega_j \sigma_j} \mathcal{I}_{1j} + \sum_{j=1}^{2} \frac{\beta k_j C_j^2 |a_j|^2}{\sigma_j^3} \mathcal{I}_{2j} + c.c., \tag{52}$$

where

$$\begin{aligned}\mathcal{I}_{1j} &= \sigma_j\delta_{bl} - \frac{\beta\sigma_j}{2} - \frac{3}{2} + \frac{1}{2}(1-\beta\sigma_j)e^{-2\sigma_j\delta_{bl}} \\ &\quad + e^{-\sigma_j\delta_{bl}}[\cos\sigma_j\delta_{bl} - \sin\sigma_j\delta_{bl}][1-\beta\sigma_j(\sigma_j\delta_{bl}+1)] \end{aligned} \tag{53}$$

and

$$\begin{aligned}\mathcal{I}_{2j} &= \frac{3}{2}(1/2 - \sigma_j\delta_{bl}) + e^{-2\sigma_j\delta_{bl}}/4 \\ &\quad - e^{-\sigma_j\delta_{bl}}[1+\delta_{bl}\sigma_j]\cos\sigma_j\delta_{bl} + 2e^{-\sigma_j\delta_{bl}}\sin\sigma_j \end{aligned} \tag{54}$$

for the shoreward mass flux, and

$$\nu = \sum_{j=1}^{2} \frac{iC_j^2 a_j^* a_{jy}}{\omega_j\sigma_j}\mathcal{J}_j + O(\beta^3) + \text{c.c.} \tag{55}$$

for the longshore directed mass flux, with

$$\begin{aligned}\mathcal{J}_j &= \sigma_j\delta_{bl} - 1 - \frac{1}{2}(1-e^{-2\sigma_j\delta_{bl}}) + e^{-\sigma_j\delta_{bl}}(\cos\sigma_j\delta_{bl} - \sin\sigma_j\delta_{bl}) \\ &\quad + \beta\Lambda_j[\frac{1}{2}(1+e^{-2\sigma_j\delta_{bl}}) + e^{-\Lambda_j\delta_{bl}}(i\delta_{bl}\sigma_j/2 - 1)]. \end{aligned} \tag{56}$$

The quantities $\mathcal{I}_{11}$, $\mathcal{I}_{21}$, and $\mathcal{J}_1$ are plotted parametrically in Figures 3, 4, and 5.

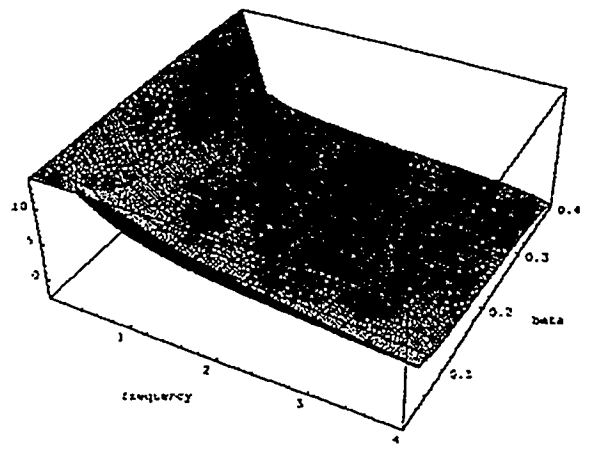

Figure 3: Variation of $\mathcal{I}_{11}$, with $\delta_{bl} = 1.0$ fixed

To summarize, then, the internal waves are obtained by solving the system

$$\begin{aligned} a_{1x} - iK_1 a_{1yy} + iK_3 f(x,y) a_1 + iK_5 e^{-i\delta x} a_1^* a_2 &= 0 \\ a_{2x} - iK_2 a_{2yy} + iK_4 f(x,y) a_2 + iK_6 e^{+i\delta x} a_1^2 &= 0 \\ a_1(x=0,y) &= \mathcal{A}_1(y) \\ a_2(x=0,y) &= \mathcal{A}_2(y) \end{aligned} \tag{57}$$

plus appropriate boundary conditions on $y = 0$ and $y = N$. The K coefficients are $O(\alpha, \varepsilon)$, and are given by Equation (34) and Equation (35). The bottom evolution, on the other hand, is Equation (50):

$$\begin{aligned} \frac{\partial}{\partial T} h(x,y,T) &= \frac{K}{\rho_0}(\mu_x + \nu_y) \\ h(x,y,0) &= \mathcal{H}(x,y). \end{aligned} \tag{58}$$

Equations (57) and (58) constitute the full model.

The solution of the system is achieved by using the following prescription: The initial bottom configuration $\mathcal{H}(x,y)$ determines the function $f(x,y)$ in Equation

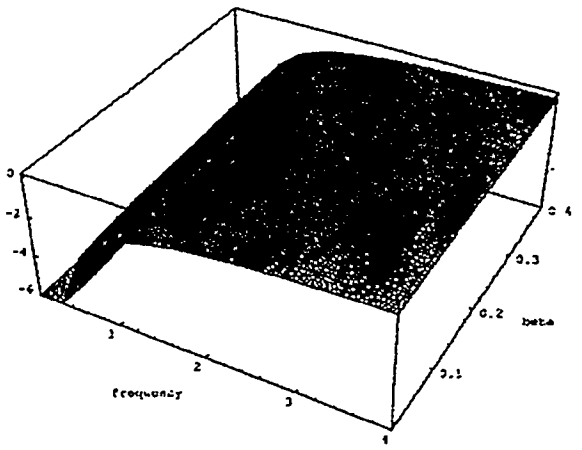

Figure 4: Variation of $\mathcal{I}_{21}$, with $\delta_{bl} = 1.0$ fixed

(57) at $T = 0$. The flow on the interface is found by solving Equation (57). The drift velocities μ and ν are computed and used in Equation (58) to update the bottom h. The new bottom is then used in the triad equations, and the whole process is repeated until some T final. If the value of T final is quite large, it could be necessary to make the boundary conditions $\mathcal{A}_i$ depend both on y and T, if the conditions that generate them are changing over time. Except for periodic updates on the boundary conditions, the prescription remains the same.

The properties of the quasi-linear hyperbolic mass transport equation are well known [Lax1973], and the existence and uniqueness of solutions ware well established: provided the initial condition $h(x, y, 0) = \mathcal{H}(x, y)$ is at least in the C^1 class of functions, and the characteristics are nowhere parallel to the manifold on which the initial data is prescribed, we have solutions in either the weak or strong sense (i.e., smooth, or shocklike). A shock solution either can be prescribed as initial data or can occur at some later time when the characteristics cross in space-time. These shocks are, in the context of sand ridge topographies, bottoms with

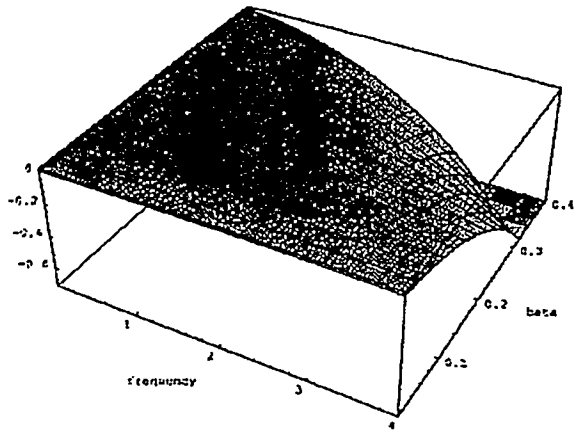

Figure 5: Parametric plot of $\mathcal{J}_1$, with $\delta_{bl} = 1.0$ fixed

sudden changes in elevation or steps. Alternatively, the bottom topographies will have wavelike features. Since either possibility exists, it is worth considering what causes either outcome.

Equation (58) may be recast as

$$\begin{aligned} \frac{\partial h(x,y,T)}{\partial T} &= K(\frac{\partial \mu}{\partial h}h_x + \frac{\partial \nu}{\partial h}h_y) \\ h(x,y,0) &= \mathcal{H}(x,y), \end{aligned} \tag{59}$$

assuming that the indicated differentiations can be performed. If in the above system we identify $\mathbf{c} \equiv (\frac{\partial \mu}{\partial h}, \frac{\partial \nu}{\partial h}) \equiv (c_1, c_2)$ as propagation speeds, we may reinterpret the problem in terms of simple wave dynamics. Assuming the solution is wavelike, it may be inferred that

$$h - \mathcal{H}(x - Tc_1(h)) = O(\alpha). \tag{60}$$

Since $\nu_y = O(\alpha)$ the second term on the right-hand side of Equation (59) affects

the outcome very minimally. Assume that $\mathcal{H}$ is differentiable. Using the implicit function theorem, we have

$$\begin{aligned} h_T &\approx -\frac{\mathcal{H}'}{1+\mathcal{H}'c_{1h}T} \\ h_x &\approx \frac{\mathcal{H}'}{1+\mathcal{H}'c_{1h}T}. \end{aligned} \qquad (61)$$

It is evident from this pair of equations that, for $c_{1h} > 0$, if $\mathcal{H}' \geq 0$ for all x, both h_T and h_x remain bounded for all time. On the other hand, if $c_{1h} < 0$ at some point, h_T and h_x diverge as $1+\mathcal{H}'c_{1h}T \to 0$. The situation is the reverse if $c_{1h} < 0$, of course. Otherwise, steplike solutions will not occur. The typical situation we have found is the latter. For such a situation it is inferred that the characteristics have wave-like dependence. Figures 6 and 7 illustrate the oscillatory nature of c_1.

Insofar as the solution of the model's system, we are concerned with the issue of stability in the iterative solution of the internal wave/bottom system, which constitutes the full model. We think of $\mathcal{H}$ as an entirely new initial condition as input to the conservation law at each value of T. We may ask then, when do the characteristics cross? Set

$$1+\mathcal{H}'c_{1h}T = 0. \qquad (62)$$

If there is crossing of the characteristics, it will occur at

$$T = -\frac{1}{\mathcal{H}'c_{1h}}. \qquad (63)$$

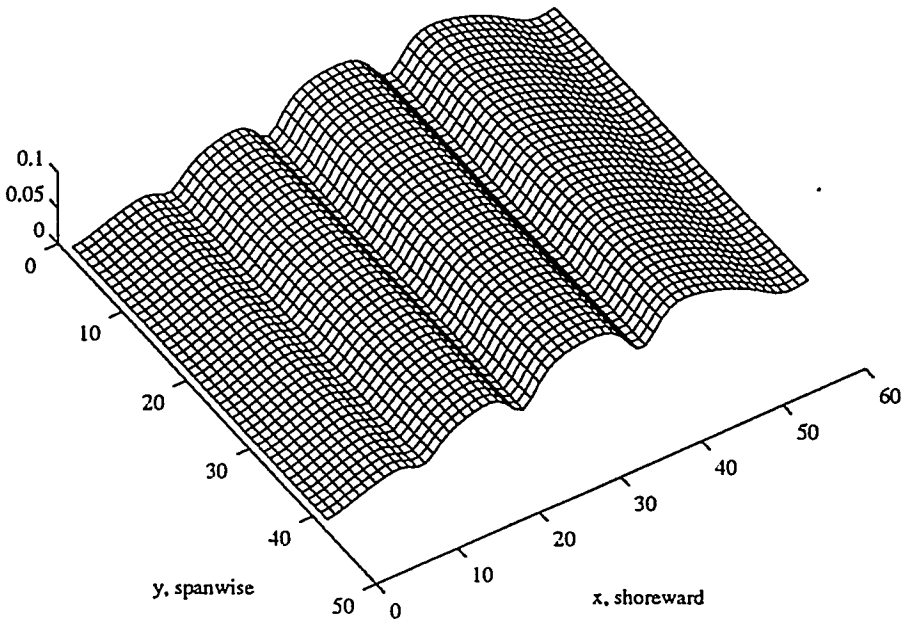

Figure 6: $c_1(T=0)$ for bottom $f(T=0) = 0.01x + 0.005y$. $\beta = 0.08$, $\varepsilon = 0.2$, $\alpha = 0.1$, $\omega_1 = 1.2$.

For the two-dimensional case

$$\begin{aligned} c_{1h} &= -\gamma_1 a_1^2 f_1(h) - \gamma_2 a_2^2 f_2(h), \\ \gamma_j &= 4K\beta^2 k_j^3 H_j/\mu_j\omega_j \\ f_j &= \gamma(1 - \frac{3}{2}\beta k_j^2 h^2); \end{aligned} \tag{64}$$

thus, crossing occurs when

$$T = \frac{1}{\mathcal{H}'[\gamma_1 a_1^2 f_1(h) + \gamma_2 a_2^2 f_2(h)]}. \tag{65}$$

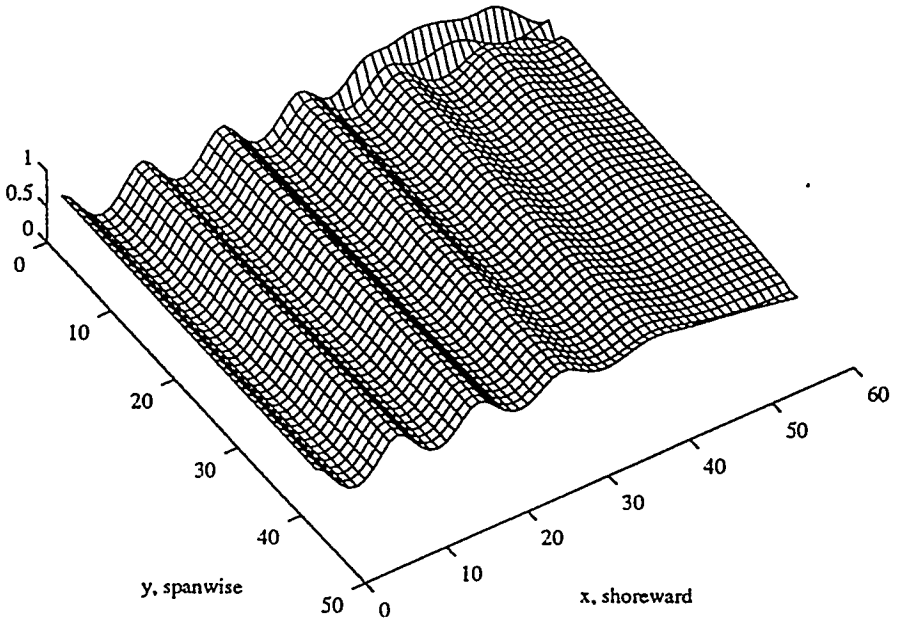

Figure 7: $c_1(T=0)$, when $f(T=0) = -0.01x - 0.005y$, $\beta = 0.1$, $\varepsilon = 0.2$, $\alpha = 0.1$, $\omega_1 = 1.2$.

By assumption, $\mathcal{H}' = O(\varepsilon) = O(\alpha)$. Since $k_j, \omega_j, K, and H_j$ are all $O(1)$, and $\mu_j = O(\beta^{1/2})$, then $\gamma_j = O(\beta^{3/2})$. Thus, an estimate for the time at which crossing may occur is

$$T = \frac{1}{O(\alpha)O(\beta^{3/2})}, \tag{66}$$

which can be quite a large interval assuming that $|a_i|$ remains bounded and less than one. This estimate applies to the three-dimensional case reasonably well since y variation is $O(\alpha)$ smaller than x variations. Note that each iterate is effectively a new initial condition for the hyperbolic equation and that the drift velocities will be different at each time step. Hence, the previous analysis does not imply

convergence of the iterative procedure but, rather, that there are constraints on the time step-size in T between iterated for the procedure to make sense.

3 Qualitative Features of the Solutions to the Full Model and Comparisons with Field Data

The main qualitative features of the full model are presented in this section, using examples computed numerically with the fixed-point method [Restrepo & Bona1993a]. To better discern the effects of different bottom topographies on the internal waves and on the eventual bottom topography after the passage of many waves, we now turn to the case in which the initial bottom configurations are strictly x-dependent and the boundary conditions are constant. Briefly, in this case, a larger number of bars form when the gradient is slight, the distance separating the bars increases seaward for the positively sloped case, and initial bottom discontinuities in the x direction tend get "smoothed out" after the passage of many waves.

Figure 8 shows the bottom topography, which was

$$f(x,y,0) = \begin{cases} 0.005x & x > 180.0 \\ 0 & \text{otherwise} \end{cases} \tag{67}$$

at $T = 0$. The lighter line represents the bottom profile at $T = 20\Delta T$; the darker line is the bottom at $T = 80\Delta T$. The parameters are $\alpha = 0.1$, $\varepsilon = 0.2$, $\beta = 0.36$, and $\omega_1 = 1.2$. For the same range of parameters, Figure 9 shows the effect on the

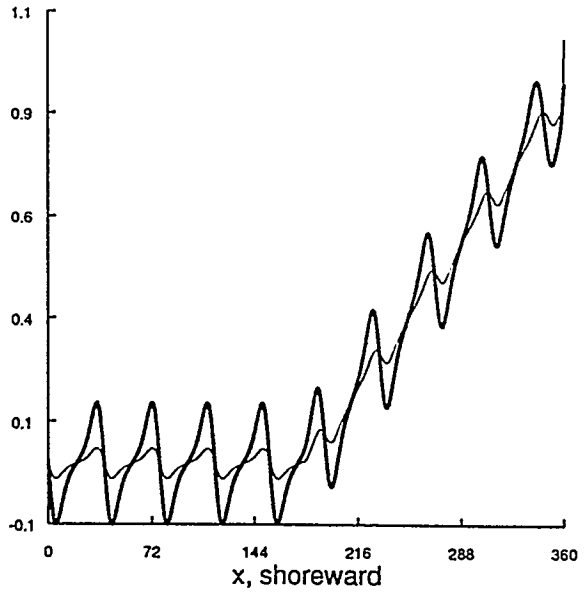

Figure 8: Cross-section of $f(x, y, T)$. The bottom was initially sloped but featureless. The darker line represents the bottom at $T = 80\Delta T$, whereas the lighter line represents the bottom at $T = 20\Delta T$.

surface and on the eventual bottom of an initial topography that is approximately tuned to the interaction length of the surface waves.

A bottom that initially had gradients in the y direction bends the water waves, affecting the eventual bottom topography by producing a series of bars with refractive features. Consider, for example, the case in which the initial bottom topography is $f(x, y) = 0.0075x - 0.005y$, the domain is $240\Delta x$ in length, and all other parameters as before. Figure 10 shows the refracting bottom at $T = 400\Delta T$. A striking way in which refraction takes place can be seen in the case for which the boundary conditions at $x = 0$ are y dependent. Shown in Figure 11 for $f(T = 400\Delta T)$ is the case for which $f(x, y) = 0$ at $T = 0$ and the boundary conditions are $\mathcal{A}_1 = 0.5 + 0.001y$ and $\mathcal{A}_2 = 0.02 + 0.001y$, corresponding to an

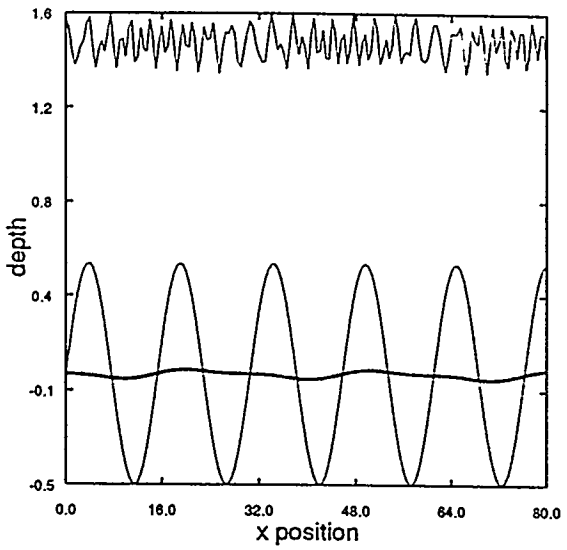

Figure 9: Effect of a tuned bottom, $f = 0.5\sin(0.412x)$ at $T = 0$, on the eventual topography and ocean surface: Light solid line. Bottom at $T = 100\Delta T$: Dark solid line.

incoming gravity wave that has slightly higher amplitude at one end than at the other.

Interesting configurations are achieved when the above-mentioned effects are combined. Figure 12 illustrates the refraction pattern on one of the modes for which $\mathcal{A}_1 = 0.5 - 0.001y$, $\mathcal{A}_2 = 0.1 - 0.001y$, and the bottom at $T = 0$ was $f(x, y) = 0.01y$.

Another curious change in pattern direction is illustrated in Figure 13. In this case $\mathcal{A}_1 = 0.5 - 0.001y$, $\mathcal{A}_2 = 0.1 + 0.001y$, and the bottom at $T = 0$ is $f(x, y) = 0.01y$. All the parameters in Figure 13 are the same as those in Figure 12.

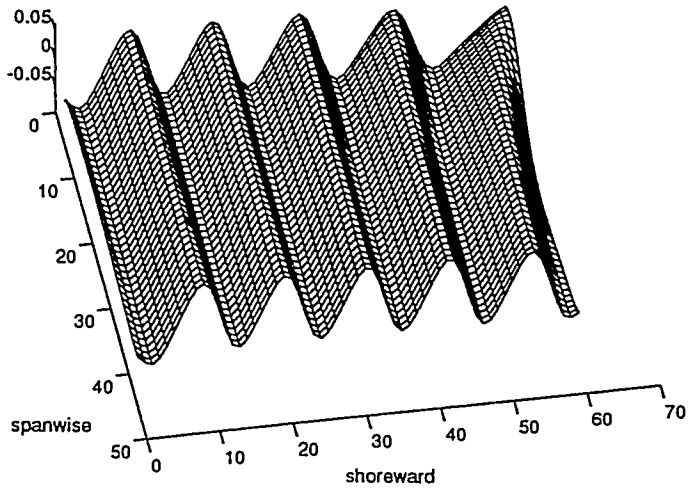

Figure 10: Refraction due to initial bottom configuration. Bottom at $T = 100\Delta T$. Shown here is the difference between the new bottom and the original topography.

4 Conclusions and Future Research Plans

This study shows how internal waves on the continental shelf, supported by the interface in a two-fluid idealization of the stratified ocean, are capable of generating structures on a sandy bottom that resemble sand ridges. It is conjectured that a significant but by no means exclusive agent for the formation and evolution of sand ridges is the second-order boundary layer drift velocity that results from the passage of overlying nonlinear dispersive waves with wavelengths that are significantly greater in extent than the local water column depth. Since the scouring action of the drift velocity has wave-like spatial structure, it produces coherent undulating patterns on the sandy bottom. While there are several types of sand ridges (and

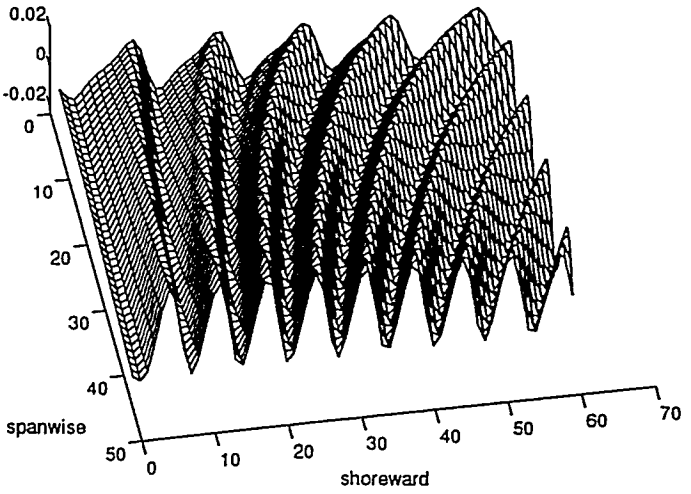

Figure 11: Refraction due to boundary conditions. Bottom at $T = 100\Delta T$.

most likely, a variety of sources for their formation), our model represents (albeit crudely) a sensible explanation for the formation of longshore sand ridges that occur on the continental shelf, far from the shoaling area, in which wave breaking is a rare occurrence and the wave field is nearly devoid of a reflected component.

While linear nondispersive gravity waves can produce a second-order drift velocity in the boundary layer hugging the bottom topography, we conjecture that weakly nonlinear dispersive water waves are more likely to be the agents of formation. The claim is that there exists a closer correlation between interbar spacing and the "interaction length" (i.e., distance in which the lowest modes of the nonlinear waves exchange their energy) rather than with the wavelength of the waves, which would be the case for linear waves.

Preliminary experimental evidence supports this claim. Boczar-Karakiewicz

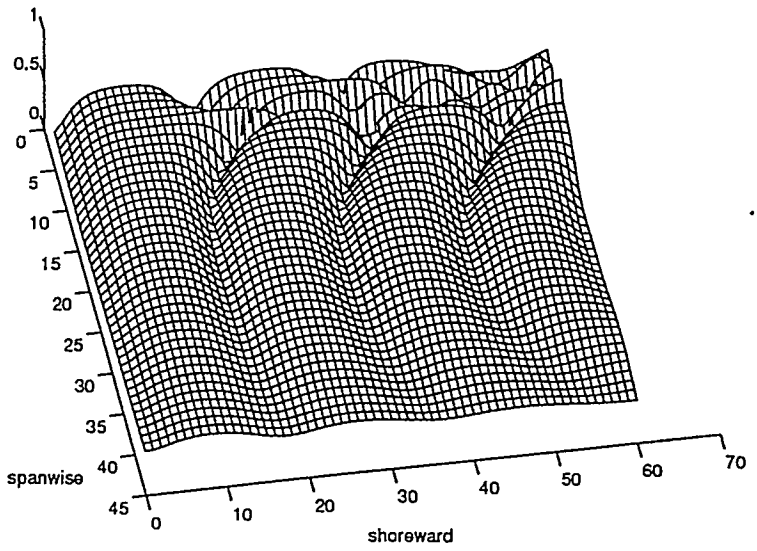

Figure 12: Refraction due to antagonistic boundary conditions and initial bottom configuration. Mode a_2 at $T = 0$.

et al. [Boczar-Karakiewicz, Paplinska & Winieki1981], in a series of experiments, were able to observe that there exists a relationship between the frequency, the amplitude, and the dispersion, in the waves and the bar spacing. As described in our model, the interaction length is a nonlinear relation that depends on the frequency, the dispersion, and the nonlinearity of the wave. Through numerical simulations it was found that the latter effect is less significant in the range of frequencies of the long shallow-water waves of the continental shelf than the dispersion [Boczar-Karakiewicz, Paplinska & Winieki1981].

The model developed here is truly evolutionary: given an initial bottom topography, it is possible to obtain the topography at some later time. An equation gives the water wave field for a particular bottom topography. Another equation,

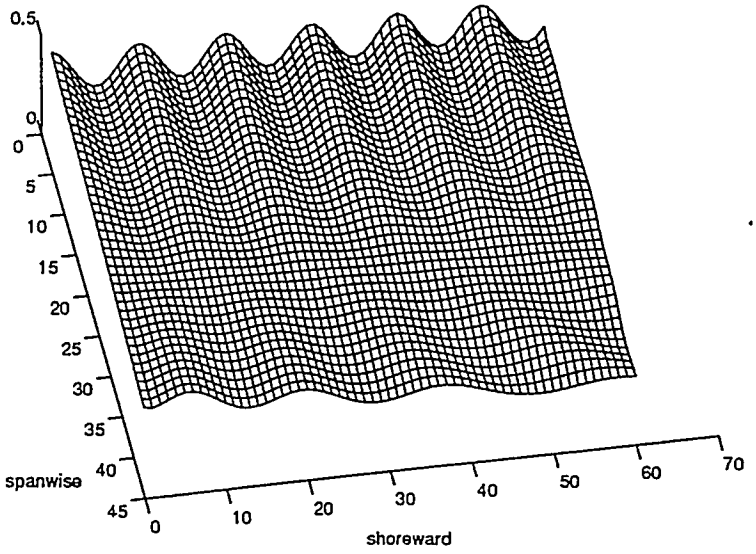

Figure 13: Refraction due to boundary conditions and initial bottom configuration. Mode a_1 at $T = 0$.

the mass transport equation, updates the topography. These equations are interdependent since the mass transport depends on the rate at which the drift velocity, which is produced by the water waves, is capable of imparting momentum to the sediment in the boundary layer, thus making changes in the bottom topography. In turn, the water waves will respond dynamically to the changes in the topography.

The iterative solution of this coupled system is enabled by the vastly different time scales in which the bottom and the waves evolve. The modal equations that yield the internal wave field are solved numerically by using a combination of finite-difference techniques and fixed-point methods. We refer to this scheme as the fixed-point method. A full description of the scheme appears in [Restrepo & Bona1993a].

The model is quite crude at this stage. The wave field is represented by its most energetic modes, and the bottom evolution equation is a simple mass balance law. We hope that further improvements in the characterization of the most relevant physical processes, such as the use of the full Boussineq system as a model for the water wave field and the parametric inclusion of sediment mechanics in the mass transport equation, will yield a great deal more structural similarity between field data and the model. Progress in our understanding of the current model and further work in gathering field data will point us in the right direction for these improvements.

An interesting question that has thus far received little attention is the subject of steady-state bottom configurations. In numerical simulations of the present model it has been observed that a common but by no means exclusive long-time outcome for the evolution of the bottom topography is one in which the structure of the modes and that of the bottom have similar qualitative features. It is also quite common in these numerical simulations for the bottom to reach its steady state in a gradual fashion rather than in small spurts of high activity followed by relative inactivity, a common observation in the formation of sand ripples [Boczar-Karakiewicz, Benjamin & Pritchard1987]. Since the temporal characterization of the evolution of actual sand ridges has not yet been systematically measured, it is difficult at present to judge whether the temporal behavior of the sand ridges created with the present model is in fact correct.

A number of interesting aspects of sand ridge dynamics require field observations. One is the measurement and characterization of the boundary layer velocities and the search for observational evidence of a periodic structure in the drift veloc-

ity that can be correlated in some way to the passing waves. Another interesting observational project is the measurement of the evolution of the spectra of internal waves in sand ridge evolution time scales, the aim being to discern how the waves change with morphological changes in the bottom topography. By far the most difficult experiment would entail the observation of the actual evolution of the bottom topography.

It is not that surprising that very little is known about sand ridges in the deeper reaches of the continental shelf from direct field measurements. While more field data is being collected and analyzed, our best recourse at present is to keep pursuing the development of models such as the one presented here. An increased understanding of its inner workings may yield clues to the dynamics of this beautiful natural phenomenon.

Acknowledgments

We thank the Applied Research Laboratory at The Pennsylvania State University for making this project possible. This work was also supported by the Office of Scientific Computing, U.S. Department of Energy, under Contract W-31-109-Eng-38.

References

Apel, J. R., "Observations of Internal Wave Signatures in ASTP Photographs," in *Apollo-Soyuz Test Project. Summary Science Report* #SP-H12, NASA, 1979, 505–509.

Baines, P. G., "Satellite Observations of Internal Waves on the Australian North-West Shelf," *Australian Journal of Marine and Freshwater Research* 32 (1981), 457–463.

Boczar-Karakiewicz, B., T. B. Benjamin & W. P. Pritchard, "Reflection of Water Waves in a Channel with Corrugated Bed," *Journal of Fluid Mechanics* 185 (1987), 229–247.

Boczar-Karakiewicz, B., B. Paplinska & J. Winieki, "Formation of Sandbars by Surface Waves in Shallow Water. Laboratory Experiments," *Rozprawy Hydrotechnisczne* (1981).

Bona, J. L., "On the stability theory of solitary waves," *Proc. Roy. Soc. London Ser. A* 344 (1975), 363–374.

Bowman, S., "Hamiltonian Formulations and Long-Wave Models for Two-Fluid Systems," unpublished, 1986.

Lax, P. D., *Hyperbolic Systems of Conservation Laws and the Mathematical Theory of Shock Waves*, Regional Conference Series on Applied Mathematics #11. Society for Industrial and Applied Mathematics, Philadelphia, PA, 1973.

Longuett-Higgins, M. S., "Mass Transport in Water Waves," *Philosophical Transactions of the Royal Society of London* 245 (1953), 535–581.

Restrepo, J. M., "A Model for the Formation and Evolution of Three-dimensional Sedimentary Structures on the Continental Shelf," Ph.D. thesis, The Pennsylvania State University, 1992.

Restrepo, J. M. & J. L. Bona, "Discretization of a Model for the Formation of Longshore Sand Ridges," Mathematics and Computer Science Division, Argonne. Ill, December 1993.

Restrepo, J. M. & J. L. Bona, "Model for the Formation of Longshore Sand Ridges on the Continental Shelf," Mathematics and Computer Science Division, Argonne, Ill, December 1993.

List of Figures